A&A 443, 383–396 (2005)
DOI: 10.1051/0004-6361:20052971

Astronomy & Astrophysics

A compact starburst ring traced by clumpy OH megamaser emission

R. Parra[1], J. E. Conway[1], M. Elitzur[2], and Y. M. Pihlström[3]

[1] Onsala Space Observatory, 43992 Onsala, Sweden
e-mail: rodrigo@oso.chalmers.se
[2] Department of Physics and Astronomy, University of Kentucky, Lexington, KY 40506, USA
[3] Department of Astronomy, California Institute of Technology, Pasadena, CA, USA

Received 2 March 2005 / Accepted 12 July 2005

ABSTRACT

We model the OH megamaser emission from the luminous infrared galaxy IIIZw35 as arising from a narrow rotating starburst ring of radius 22 pc enclosing a mass of 7×10^6 $M_\odot$. We show how both the compact and apparently diffuse maser emission from this ring can arise from a single phase of unsaturated maser clouds amplifying background radio continuum. The masing clouds are estimated to have a diameter of <0.7 pc and internal velocity dispersion of ~20 km s^{-1}. We find that the clouds are neither self-gravitating nor pressure confined but are freely expanding. Their dispersal lifetimes may set the vertical thickness of the ring. For an estimated internal density of 3×10^3 cm^{-3}, cloud masses are of order 24 $M_\odot$. The observed spectral features and velocity gradients indicate that the clouds must be outflowing and escaping the nucleus. The cloud mass outflow rate is estimated to be 0.8 $M_\odot$ yr^{-1}, while the star formation rate is ~19 $M_\odot$ yr^{-1}. Associated ionised gas, possibly generated from dissipated clouds, provides free-free absorption along the source axis, explaining the observed East-West asymmetries. We show that the clumpiness of a maser medium can have a dramatic effect on what is observed even in a relatively low gain OH megamaser. Specifically, in IIIZw35 our clumpy maser model naturally explains the large line to continuum ratios, the large 1667 MHz:1665 MHz line ratios and the wide velocity dispersions seen in the compact maser spots. Other astrophysical masers showing both compact and apparently diffuse emission might be explained by similar clumpy structures.

Key words. galaxies: starburst – galaxies: individual: IIIZw35 – masers

1. Introduction

Extra-galactic OH megamaser emission is generally associated with compact (<100 pc scale) starburst or AGN activity in the centres of IR luminous galaxies. Observations of this maser emission provides a unique method of studying the structure and kinematics of galactic nuclei at parsec resolution without dust obscuration effects. Measurements of velocity gradients and line widths (e.g. Pihlström et al. 2001, hereafter P01) already provide important constraints on stellar mass densities and turbulent velocities in IR luminous galaxies. Such observations may also trace large scale obscuring tori in composite AGN/starburst sources (Klöckner et al. 2003). Potentially OH megamasers can also tell us about the size, density and temperature of molecular clouds in the central ISM of starburst galaxies and AGN. However, to accomplish these goals a better understanding of the OH megamaser phenomenon is required.

Recent MERLIN and VLBI observations of OH megamasers have suggested that the standard model, developed in the 1980s (Baan 1989), might need modification (see Lonsdale 2002 for a review). In this standard model OH maser emission is generated by low gain ($|\tau| \lesssim 2$) unsaturated amplification of background continuum by a foreground OH amplifying medium. Although this medium is comprised of discrete OH clouds it is implicitly assumed that there are many such clouds and they individually have very low gains. These clouds therefore form an effective gas in which statistical fluctuations in cloud number between different lines of sight are unimportant and so the maser opacity varies slowly across the source. Given these assumptions the amplifying medium is often described as a diffuse screen.

Consistent with the standard model early VLA and MERLIN observations showed that OH maser and continuum emission overlapped. Since both continuum and maser emission were assumed to be smooth on scales $\lesssim$100 pc VLBI observations were not expected to reveal anything interesting. However, when VLBI observations were finally made of Arp220, both compact continuum (Diamond et al. 1989; Smith et al. 1998) and compact OH maser emission were detected (Lonsdale et al. 1994, 1998, hereafter L98). Remarkably, the

bright maser spots in Arp220 were not coincident with the continuum spots, and some maser spots displayed extreme line-to-continuum ratios (i.e. >800 in L98). These observations were clearly inconsistent with diffuse screen models. Slightly less extreme compact maser emission was subsequently detected in other sources (Trotter et al. 1997, hereafter T97, Diamond et al. 1999, hereafter D99; Klöckner et al. 2003; Klöckner & Baan 2004). These same sources also contain diffuse maser components which account for between 50% and 90% of the total maser flux density. It has been suggested that the compact masers occur in saturated, perhaps collisionally pumped regions, while the diffuse component comes from an extended unsaturated, radiatively pumped screen fully consistent with the standard model (L98, D99).

One of the clearest cases of an OH megamaser showing both compact and diffuse maser emission is IIIZw35. Two groups of compact masers were detected in VLBI observations (T98, D99), but only about half of the total OH maser emission seen on MERLIN scales (Montgomery & Cohen 1992) was recovered in the VLBI maps. To determine the location of this missing component P01 conducted EVN+MERLIN observations. These observations revealed perhaps the best example of a rotating OH maser ring yet found. The previously known compact masers lie at the tangents of this ring. Such a location is hard to understand if compact and diffuse masers are generated by different physical mechanisms. Instead, a geometrical origin for the compact masers is suggested. P01 proposed a mechanism based on a single phase of OH masing small clouds (∼1 pc). At the ring tangents multiple overlaps between clouds in space and velocity are likely due to the increased path length through the ring. These multiple cloud overlaps give rise to the bright compact maser features. Elsewhere, at the front and back of the ring where there are few such cloud overlaps, the emission consists of many weak maser spots. These spots are too weak to be detected individually in high resolution observations but in low resolution observations they are averaged together and give rise to an apparently diffuse emission.

In this paper we investigate in greater depth the clumpy ring model proposed in P01. Here we fully consider the spectral properties of the clouds and their velocities are treated in a more realistic way. We also model the continuum emission in a geometrically and physically consistent manner. Using numerical simulations we demonstrate that most of the available OH maser observations of IIIZw35 can be explained using an improved version of the P01 model. Most of the input parameters for these simulations are constrained directly by the observations. Our modelling also illuminates general properties of maser ring geometries and clumpy maser media.

The detailed plan of this paper is as follows. Section 2 summarizes the relevant observations of IIIZw35. In Sect. 3 we present the clumpy ring model and derive its parameters. Section 4 describes the numerical simulations and compares the results of the simulations with observations. Section 5 presents a general discussion on how the observed maser characteristics can be explained by a clumpy medium. In Sect. 6 the derived physical properties of the clouds and the galactic nucleus are discussed. Finally in Sect. 7 we draw conclusions and suggest future work.

2. Source properties and observations

IIIZw35 is a Luminous Infra-red Galaxy ($L_{\rm FIR} = 10^{11.3}\,L_\odot$) at a distance of 110 Mpc (assuming $H_0 = 75$ km s^{-1}Mpc^{-1}, (Chapman et al. 1990, hereafter C90)) which gives a linear scale of 0.5 pc mas^{-1}. From optical spectroscopy it has been classified as a borderline LINER/Seyfert 2 (C90). The galaxy lies on the well known radio-FIR correlation and both the radio continuum and IR emission are consistent with being powered by a starburst with a star formation rate (SFR) of ∼19 $M_\odot$ yr^{-1} (P01). Both the 1667 MHz and weaker 1665 MHz megamaser emission were discovered by Staveley-Smith et al. (1987). The ratio of peak opacities in the 1667:1665 MHz spectra is ∼9 (Staveley-Smith et al. 1987; Mirabel & Sanders 1987), which is at the higher end of observations amongst OH megamaser galaxies (Henkel & Wilson 1990). From single dish CO observations, Mirabel & Sanders (1987) estimate an overall molecular gas mass of 6.5×10^9 $M_\odot$. The dynamical mass within a radius of 22 pc is estimated by P01 to be $\sim 7 \times 10^6$ $M_\odot$, implying that most of the molecular gas is located in a more extended structure.

Intermediate resolution maps of the OH maser emission have been produced by P01 by combining EVN and MERLIN datasets and are reproduced in Fig. 1. The greyscale in Fig. 1a shows that, at this resolution, the maser emission has a clear void near its centre and two bright regions to the North and South, with an estimated Line-to-Continuum Ratios (LCR) of 47 ± 13 and 73 ± 8 respectively. Two bridges of diffuse emission connecting the bright regions can also be seen. Although the one to the West is brighter, it has the smaller LCR; the western bridge has LCR = 9 ± 2, the eastern bridge has an LCR = 14 ± 4. Figure 1b shows the North-South velocity gradient obtained from the maser moment map. This gradient and the maser brightness distribution, are consistent with a rotating ring whose axis is inclined by $i \sim 60^\circ$ from the direction of the observer. The bright North and South regions are interpreted as arising from the tangents of the ring, where path lengths are longer, while the bridge emission originates at the front and back sides of the ring (see Fig. 2). At VLBI resolution (T97, D99), the diffuse bridges are not detected while the two bright regions break up into complexes of bright maser spots. In one of the spots the inferred LCR is >500 (D99). In general the spots are unresolved, thus having sizes of less than 0.7 pc (D99). Spot spectral widths are measured to be 30−50 km s^{-1} (D99). Both, T97 and D99 find that the spot velocity centroids trace a roughly East-West gradient within the northern region. Approximately half of the velocity integrated line flux density seen in Fig. 1a within the northern and southern regions comes from the compact spots, the rest is not detected at either VLBA (T97) or global VLBI (D99) resolution.

In addition to the OH maser emission P01 also detected continuum emission in their EVN+MERLIN data (see contours in Fig. 1a). In contrast at global VLBI resolution only upper limits to the continuum have been found (T97; D99), implying that most of the continuum emission is smoothly distributed. The continuum emission seen at EVN+MERLIN resolution, just like the OH emission, is stronger on the western side of

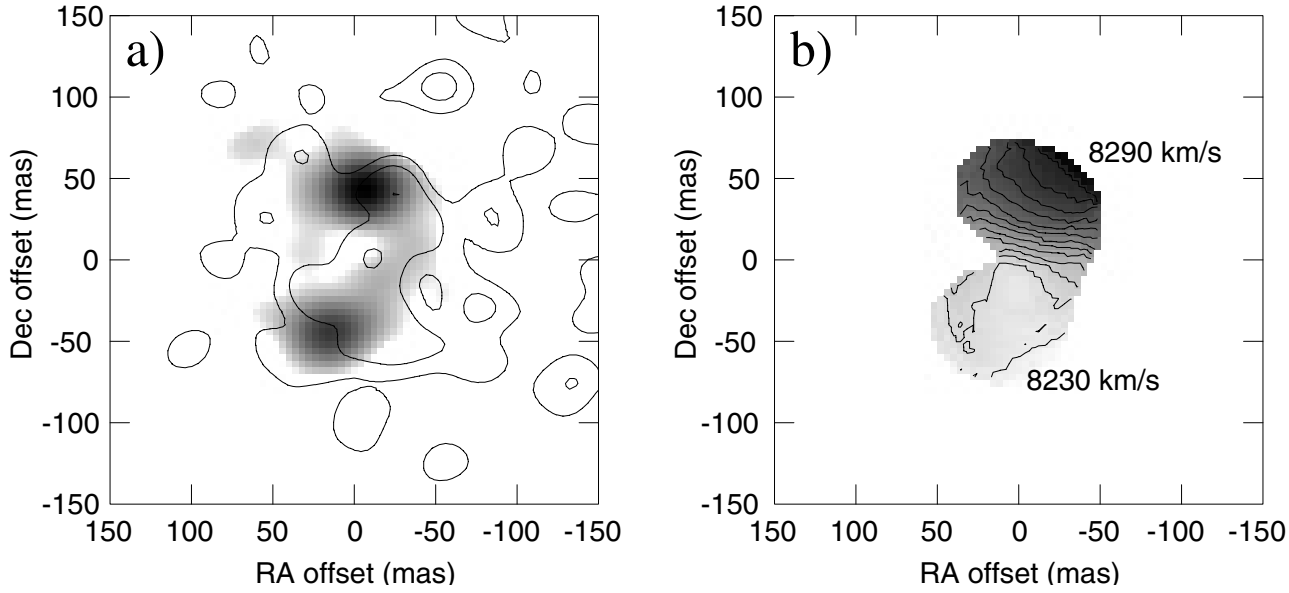

Fig. 1. Images reproduced from P01 showing observations of OH maser and continuum emission at EVN+MERLIN resolution **a)** Greyscale shows the velocity integrated OH emission at a resolution of 34 × 29 mas. The contours show continuum emission at the same resolution. Contour levels are at –1, 1, 2, and 4 times the 3σ noise of 0.42 mJy/beam. **b)** Corresponding OH maser velocity centroid field. The greyscale is between 8224 (lightest grey) and 8300 km s^{-1} (black). Contours are from 8230 km s^{-1} increasing at 5 km s^{-1} intervals up to 8290 km s^{-1}.

the source and is therefore asymmetrically distributed about the major axis of the inferred OH maser ring.

3. Clumpy ring model

3.1. Overall geometry

In this paper we fit the IIIZw35 observations by an inclined axisymmetric model in which both OH clouds and continuum emission coexist within circumnuclear rings (see Fig. 2). To reconcile such a symmetric geometry with the observed East-West asymmetry in both line and continuum emission (see Fig. 1a) our model also includes a bi-cone of free-free absorption which covers the eastern side of the source. This obscuration defines the maser ring orientation requiring the eastern side to be the most distant. Note that the existence of a free-free absorbing component is supported by independent evidence. C90 found that the integrated radio spectrum has a turnover at ∼1 GHz. Given the size of the radio emission this cannot realistically be due to synchrotron self-absorption, because enormous departures from particle/field equipartition would be needed. Physically the free-free absorbing cone could be the base of an outflowing superwind such is often observed in energetic starbursts (Heckman 2003).

As noted in Sect. 2 although the total maser emission is weaker on the eastern side the LCR is about factor of 2 larger there than on the western side. This difference is explained if more of the seed continuum emission is background to the OH ring on the east side. This naturally occurs if most of the bright continuum emission comes from a larger radius than the OH masing gas (see Fig. 2a). This is corroborated by the fact that the observed continuum radio source is larger than the megamaser source (see Fig. 1a). As shown in Sect. 4.3 this geometry also predicts that the brightest masers do not occur exactly at the maser ring tangents but slightly to the east of the tangent points, just as found by the observations of T97 and D99.

The detailed properties of the different components of the model are estimated in the following subsections and summarised in Table 1. These parameters are used in the Monte-Carlo simulations described in Sect. 4.

3.2. Free-free absorption bicones

From the observed ratio of the continuum emission brightness on the East and West sides of the source, the line of sight opacity through the cone to the eastern bridge is estimated to be ∼0.7 at the observing frequency. Since all of the eastern bridge emission is weak compared to the western bridge the opening angle of the bicone must be significant. We therefore assume a bicone in which the opacity per unit length decreases with angle from the symmetry axis as a gaussian with *FWHM* 60°.

3.3. Ring dimensions

The dimensions of the region containing the OH masing clouds are shown in detail in the right panel of Fig. 2. This thin ring structure has inner radius $R_{\rm in}$ and an outer radius $R_{\rm out} = R_{\rm in} + \Delta R$. P01 find that $R_{\rm in} \sim 22$ pc. From the North-South extent of the region covered by bright maser spots in the VLBA and global VLBI maps (T97 and D99), ΔR is ∼3 pc. From its East-West extent near the ring tangents we infer a ring height of $\Delta H \sim 6$ pc. The aspect ratio of the projected ring shows that the ring axis is inclined at angle $i \sim 60°$ from the observer's direction (P01). We find that an axisymmetric continuum emissivity profile which peaks at radius $R_{\rm c} = 37$ pc best fits the continuum observations (see Fig. 1a and Sect. 4.2). We also find that the

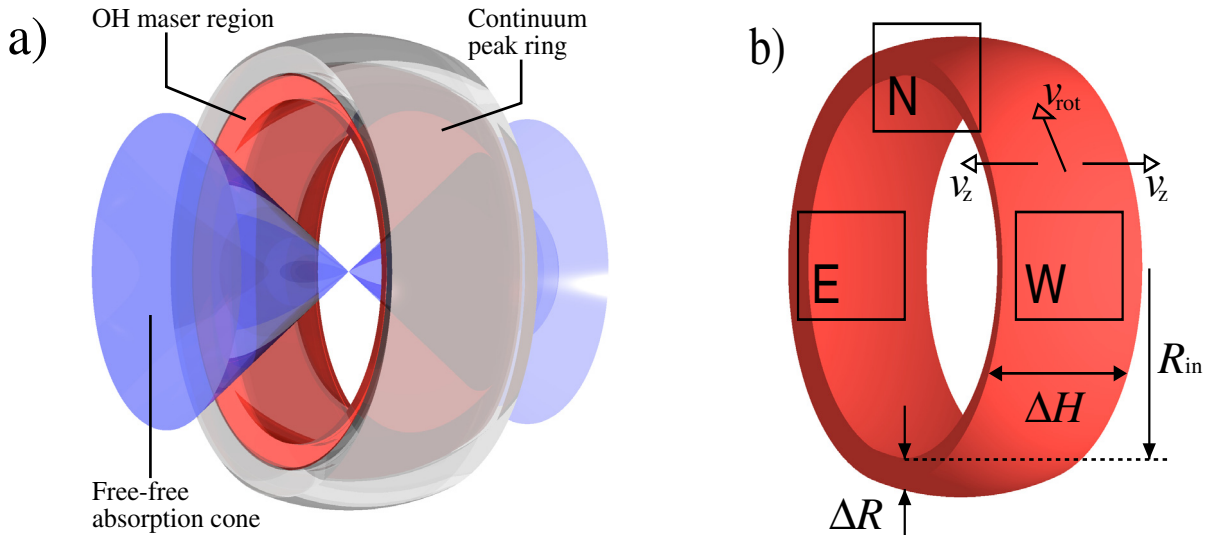

Fig. 2. a) Sketch of the proposed source geometry. The inner dark grey ring represents the region where OH masing clouds are confined. The outer light grey ring depicts an isosurface of the smoothly distributed continuum emissivity. Note that although the radius of peak continuum emissivity lies outside the OH maser ring, some continuum emission interpenetrates and even lies within the OH ring (not shown in this figure). This geometry explains the large line to continuum ratio on the eastern side of the source because here the majority of the continuum is background to the OH. In contrast on the western side only the smaller fraction of the continuum which interpenetrates and lies inside the OH maser zone is available as a source of seed photons. In order to explain the relative weakness of the absolute brightness of both line and continuum on the eastern side of the source (see Fig. 1) the model also includes a region of free-free absorption within a bicone which covers the eastern side of the source. **b)** Detailed representation of the OH maser ring indicating positions and dimensions referred to in the main text. Arrows indicate components of cloud rotation around the ring (v_{rot}) and outflowing from the ring midplane (v_z). See Sect. 3.6 for more details.

Table 1. Model parameters

Maser and continuum ring properties:	
Maser ring inner radius $R_{in}{}^a$	22 pc
Maser ring radial thickness ΔR^a	3 pc
Maser ring height ΔH^a	6 pc
Maser ring Rotation velocity v_{rot}^b	57 km s^{-1}
Continuum peak emissivity radius $R_c{}^b$	37 pc
Inclination angle i^b	60°
Free-free absorption bicone properties:	
Opacity τ_{ff}	0.7
Opening angle (*FWHM*)	60°
Cloud properties:	
Cloud size a^c	<0.7 pc
Internal velocity width $\delta v^{c,d}$	20 km s^{-1}
Random velocity dispersion $\Delta v^{c,d}$	60 km s^{-1}
Outflow velocity v_z	60 km s^{-1}
Outflow velocity dispersion Δv_z^d	30 km s^{-1}
Number of clouds along radius N_0	1.8
Cloud volume filling factor f	<0.08
Cloud maser optical depth τ_c	1.5

Refs: [a]T97; [b]P01; [c]D99;
[d] The dispersions represent the *FWHM* of a Gaussian probability distribution.

continuum emissivity function must be relatively wide in radius so that not all of the continuum lies outside the OH maser region.

3.4. Need for a single-phase clumpy medium

Having constrained the geometry of the maser emitting zone we now argue that it must consist of distinct clouds. Maser amplification of background continuum gives LCR = e$^{\tau}$, where τ is the maser optical depth. When the amplification is due to a smooth distribution of uniform unsaturated maser gas, τ is proportional to the path-length through the region. The ring geometry derived in the previous sections implies a factor of 8 difference between the maximum path-lengths in regions N and E (see Fig. 2) such a ratio in path length implies $LCR_N = (LCR_E)^8$. In contrast, the ratios observed at EVN+MERLIN resolution are $LCR_E \sim 12$ and $LCR_N < 75$, a conflict of at least four orders of magnitude with this relation. The problem becomes even worse if saturation affects the bright features because the optical depth of a saturated maser is always larger than that of an unsaturated maser of the same length.

In contrast with a smooth maser screen, a collection of independent clouds involves a statistical effect, predicting a variation in LCR with position around the ring which can match the EVN+MERLIN observations. As described in the appendix, a remarkable property of clumpy media is that the effective opacity is not linearly proportional to the path length, instead it falls below the linear prediction. This result gives a compelling argument for the OH masers occurring in clouds. This argument is separate and additional to the one proposed in P01 which required clouds to explain the brightest spots by multiple cloud overlaps.

3.5. Cloud properties

Based on the high resolution observations of the brightest maser spots in D99 maser spot diameters are estimated to be $\lesssim$0.7 pc. In general the spot size associated to a high gain maser is smaller than the size of its originating maser cloud (by a factor of $\sim\sqrt{\tau}$). However since the maser opacity of the clouds employed in our model is about one (see below) the size of the maser produced by a single cloud is about the same size of the cloud. In spots caused by multiple cloud overlaps the apparent reduction in size caused by increased opacity is counteracted by the widening due to spatial misalignments. The cloud size is therefore estimated to be the same as that set by spot size, <0.7 pc. A lower limit for the cloud size is set from physical arguments (see Sect. 6.1). For our Monte-Carlo simulations (Sect. 4) we adopt the observed upper limit as the actual cloud size but argue that our results are only weakly dependent on the exact size chosen.

From the observed velocity widths of the bright maser spots (D99) cloud internal velocity dispersions of order 20 $\mathrm{km\,s^{-1}}$ are implied. Again a similar argument applies in velocity as in space to explain why we expect observed and true cloud velocity widths to be similar. Values for the cloud number density and opacity were found from the Monte-Carlo simulations. As described in Sect. 4.1, the initial starting point for this search was guided by the observed LCR distribution around the ring (see Sect. 3.4) and the theory developed in the appendix. The best fit was obtained assuming a cloud opacity of $\tau_c = 1.5$ and a volume number density such that the number of clouds along a radius in the disk plane at any velocity was $N_0 = 1.8$. For a cloud size of $a < 0.7$ pc this implies, averaged over the OH maser ring, a cloud volume filling factor $f < 0.08$. As we argue in Sect. 4.1 our fits to the data are expected to remain similar as a function of a as long as the cloud number density is adjusted to maintain a constant N_0. In this case the cloud volume filling factor will scale with cloud size as $f = 0.08(a/0.7\,\mathrm{pc})$.

3.6. Velocity field

Observations show (see Fig. 1b) a large scale North-South gradient in maser velocity centroid consistent with ring rotation. Note however that the velocity dispersions within the bright northern and southern tangent regions are comparable to the rotation velocity so that the integrated spectra from the two regions overlap (see P01 and T97). At higher resolution global VLBI observations show within the northern tangent region a clear velocity gradient which is almost East-West. This small scale gradient is almost parallel to the projected ring axis and almost at right angles to the gradient found on large scales.

The observed large scale gradient can readily be fitted if the clouds are assumed to have an orbital velocity component (see Fig. 2b) of $v_{\mathrm{rot}} = 57$ $\mathrm{km\,s^{-1}}$ (P01). Somewhat harder to explain is the gradient seen within the northern tangent region. Part of this gradient can be explained by the ring rotation. The brightest masers are not found exactly at the OH maser ring tangents but slightly to the East where there is more background continuum (see Fig. 2a) and the orbital velocity gives a small velocity gradient along the ring. This mechanism cannot however explain the magnitude of the observed gradient. Instead we propose that clouds, in addition to their rotation velocity, have a comparable outflow velocity (v_z, see Fig. 2b) which is parallel to the ring axis and directed away from the disk midplane. To see how this gives the observed gradient consider a cloud near a tangent region in Fig. 2b. If such a cloud lies above the ring midplane (near side), the cloud will be located to the East of the tangent point and its projected outflow velocity will be blueshifted. On the other hand if it lies below the ring midplane (far side) the cloud will be located to the West of the tangent point and its projected outflow velocity will be redshifted. This mechanism can produce an apparent East–West velocity difference of nearly twice the projected outflow velocity within a small distance comparable to the maser ring height.

It is interesting that at the northern tangent the cloud outflow mechanism gives a velocity gradient in the same direction as that caused by the rotation mechanism, thus reinforcing the gradient. In contrast in the South the gradients from the two mechanisms have opposite directions and will partly cancel. This may explain why an East-West gradient is only seen in the North. Alternatively the difference may mainly be due to the statistical nature of our clumpy maser model. We have found using Monte-Carlo experiments (see Sect. 4) and assuming an outflow velocity of $v_z = 60$ $\mathrm{km\,s^{-1}}$ and dispersion $\Delta v_z = 30$ $\mathrm{km\,s^{-1}}$ that small scale gradients of the required amplitude often arise in the tangent regions, with the northern region being favoured.

While the outflow velocity component contributes significantly to the high velocity dispersion seen at EVN+MERLIN resolution we also find from our Monte-Carlo modeling that an additional cloud random velocity component of dispersion $\Delta v = 60$ $\mathrm{km\,s^{-1}}$ is required. In particular this random velocity component is needed to fit the observed very wide velocity dispersion of the northern and southern tangent regions at EVN+MERLIN resolution.

4. Modelling and results

In this section we calculate in detail the emission from the clumpy maser ring using Monte Carlo simulations. In Sect. 4.1 we present the details of the model. In Sect. 4.2 we explain how we compute our synthetic OH maser cubes and continuum images. Finally in Sect. 4.3 we compare our results with observations.

4.1. Model details

Our numerical model contained three components (see Sect. 3.1): a high brightness temperature radio continuum emission to provide seed photons for maser amplification, a free-free absorbing cone and a randomly distributed population of OH masing clouds. The continuum component was modelled as a radially smooth axisymmetric emissivity function. This function was chosen to have peak emissivity at radius R_c (see Table 1) and its shape was chosen so that it approximately matched the P01 continuum image (see Fig. 1a). The bi-cone of free-free absorption (see Fig. 2a) was assumed to have a density obeying a Gaussian distribution of $FWHM = 60^\circ$ around

the ring axis producing a total opacity of $\tau = 0.7$ toward the eastern bridge region (see Sect. 3.2).

The maser clouds were assumed to be identical and spherically symmetric with a number density of maser molecules described by a three dimensional Gaussian distribution with a *FWHM* of 0.7 pc (see Sect. 3.5). For computational reasons this density profile was cutoff beyond a radius of 1pc. The corresponding cloud internal velocity profile was assumed to be a Gaussian with *FWHM* $\delta v = 20\,\mathrm{km\,s^{-1}}$.

As discussed in Sect. 6.1 the clouds could be physically smaller than the above *FWHM* of 0.7 pc and still give the required maser opacity. Fortunately we find that when the clouds are small enough to be unresolved by the highest resolution interferometer beam the model results are only very weakly dependant on the actual cloud size used. As described in the appendix the critical parameters for determining structure are the cloud opacity τ_c and mean number of clouds per line of sight $\bar{N}$. If a smaller cloud size was used and consequently the volume density of clouds increased to maintain the same $\bar{N}$, then the results to first order would be the same. The only explicit dependence on cloud size is via the inverse Poisson function (see appendix) which is an extremely weak function of the number of independent lines of sight (M); a quantity which in turn is inversely proportional to the cloud area. The effect of using clouds much smaller than used in our simulations would be to make the peak line to continuum and 1667:1665 MHz line ratio somewhat larger, but as we shall see (see Sect. 4.3) these ratio limits are well fitted even when using the largest possible cloud size.

As described in Sect. 3.6 the cloud bulk motions comprise orbital, outflow and random components. To implement these motions in our simulations we first found for each cloud six orbital parameters for a random orbit around the gravitational potential induced by the $7 \times 10^6\ M_\odot$ enclosed mass. The maximum allowed orbit inclination was set to the ratio $\Delta H/2R_{\rm in}$. Clouds were also constrained to lie within an annulus with inner and outer radii $R_{\rm in}$ and $R_{\rm out} = R_{\rm in} + \Delta R$ (see Table 1). The outflow from the ring plane (see Sect. 3.6) was simulated by adding a velocity component parallel to the ring axis to each cloud. After experimenting it was found that assuming a mean $v_z = 60\,\mathrm{km\,s^{-1}}$ with dispersion $\Delta v_z = 30\,\mathrm{km\,s^{-1}}$ directed away from the ring plane, plus a random 3D velocity of $60\,\mathrm{km\,s^{-1}}$ gave acceptable results. This velocity field produced realisations which showed velocity gradients within the northern tangent region and could also match the observed velocity dispersion.

As described in Sect. 3.5, the volume number density of clouds N_c and their opacity τ_c were left as adjustable parameters within the Monte-Carlo simulation. To guide the search for these parameters we utilised the formalism developed in the appendix. A system of two equations was set up using the expressions for the beam-averaged gain over the northern and eastern regions. The system was solved in the least-squares sense subject to a lower-bound constraint established by the observed peak gain at global VLBI resolution. The optimum solution found had $\tau_c = 1.5$ and a cloud number density in the midplane of $N_c = 0.2\ \mathrm{pc^{-3}}$. For this density the number of clouds intersected at any velocity by a radial equatorial ray is $N_0 = 1.8$. The required number density was achieved in our simulations by using 1200 clouds.

4.2. Model computation

Maser emission was calculated by ray tracing for each line of sight (LOS) and velocity taking into account the amplification of continuum seed photons by the interspersed maser clouds. Synthetic spectral line data cubes and continuum images were produced and convolved with appropriate beams for comparison with observations. The simulations were run in a dual Pentium III 1.5 GHz computer with 2 GB of RAM running Linux. A realisation using a synthetic cube of size 201^3 with 1200 clouds took approximately 20 min. An important aspect of our implementation is that for each realisation, the cloud information is stored as a list of real numbers (and not gridded), so it is relatively easy and efficient to recompute the expected emission at different resolutions by specifying different grid sizes.

4.3. Results and comparison with observations

A set of 100 simulations were run using the parameters given in Table 1. The maser and continuum emission from a typical realisation are shown in Fig. 3 in a way that can be directly compared to the observations in Fig. 1. Relevant numerical results for this realisation compared to observations are given in Table 2. The model continuum emission shown by the contours in Fig. 3a matches well the high brightness regions of the observed continuum (compare to contours in Fig. 1a). It is clear that our continuum model does not include the very extended emission present in the observations. However we consider that this model is sufficiently accurate for our main purpose of calculating synthetic OH maser emission cubes.

The greyscale in Fig. 3a shows the integrated OH maser emission from our model and it can be seen to be very similar to the observations (compare to Fig. 1a). Figure 3b shows the model velocity field obtained from the moment map of the OH emission. Again, its overall structure agrees quite well with observations (compare to Fig. 1b). There is a North-South asymmetry in the model velocity field which in this realisation is partly caused by the presence of a single bright maser feature in the South. The outflow velocity given to the clouds also contributes to break the North-South symmetry (see Sect. 3.6). The observations (Fig. 1b) show a similar but larger asymmetry between North and South. This might be explained by the fact that in the observations the south contains an even more dominant single spot than is the case in the model. Additionally note that the model moment map is produced using all the maser emission from the high resolution cube whereas in the observations there may be a resolved-out component not included in the average.

In order to show the range of structures produced in the Monte-Carlo simulations Fig. 4 displays three selected realisations of the model and the average over the entire set. The top two rows show velocity-integrated images at MERLIN+EVN and global VLBI resolutions, the bottom row shows the

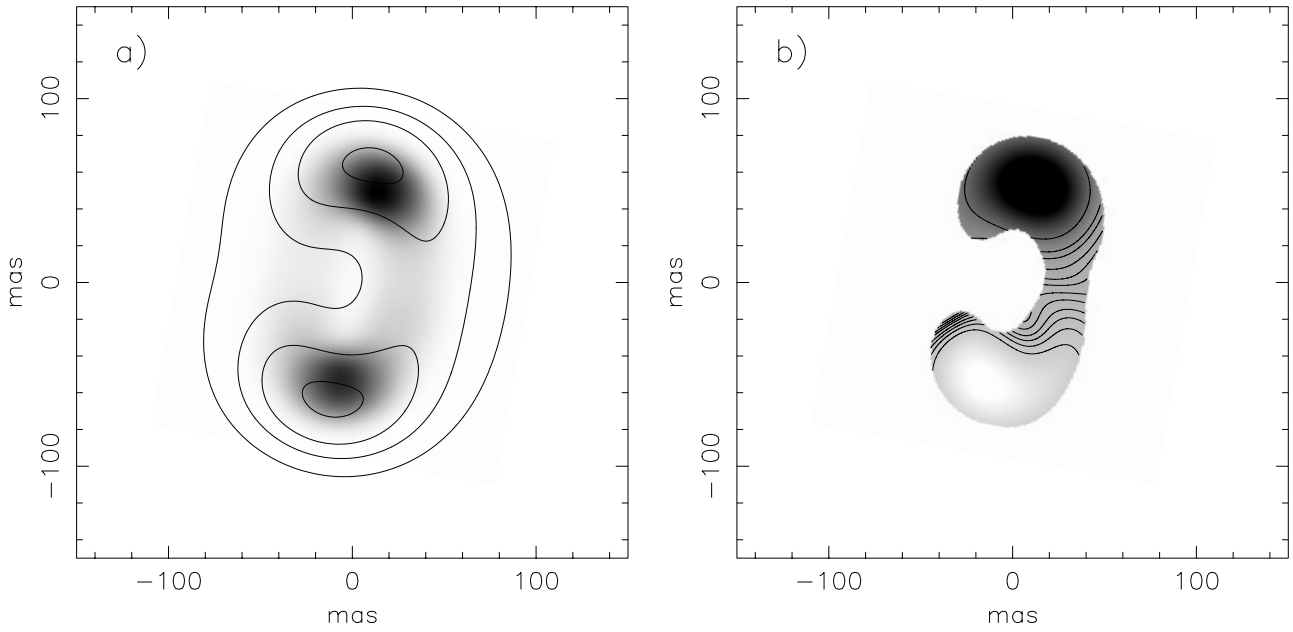

Fig. 3. a) Model continuum emission superimposed on the velocity integrated OH maser emission. The contours, greyscale and the resolution are equivalent to those in Fig. 1a. **b)** Corresponding modelled OH maser velocity centroid field. Greyscale is between –60 and 60 km s^{-1} around the systemic velocity. Contours are from –30 km s^{-1} and increasing by 5 km s^{-1} up to 30 km s^{-1}. Compare with Fig. 1b.

corresponding integrated spectra. As expected, the simulations show bright emission at the tangent regions and diffuse emission in between. The intensity is lower in the eastern bridge due to the effect of the free-free absorbing cones, yet the LCR is higher there, reflecting the relative locations of the maser clouds and radio continuum. From Table 2 we see that the values obtained for the EVN+MERLIN optical depths in the bridges are somewhat less than observed. This may be due to the fact that the model uses only one type of spherical cloud representing a whole population that certainly has various sizes and optical depths. The bridge regions have small effective optical depths and can be expected to be more strongly affected by fluctuations, which are amplified exponentially, around the mean cloud optical depth. At global VLBI resolution (Fig. 4, middle row) the bright tangent emission breaks up into numerous compact maser spots due to multiple cloud overlaps. With the greyscale level chosen there are more such spots on the western side of the projected ring major axis, this is caused by the effect of the free-free absorbing bicone.

The single dish model spectra (Fig. 4, bottom row) agree in shape and velocity width with the Staveley-Smith et al. (1987) observations. The spectra averaged over the northern and southern tangent regions (dashed and dotted lines) are also similar to those found by T97, including the velocity overlap of the two regions; this overlap is due to the large cloud velocity dispersion (comparable to the orbital velocity) included in the calculations. The emission from the northern and southern tangent points comprises about half of the total emission, as found in T97. The remaining missing flux comes from the eastern and western bridges of smooth emission mostly centered on the systemic velocity, as found in P01. The last column of Fig. 4, representing the average over all the 100 realisations, shows that the model is stable. That is to say that the main structures produced, which match observations, are typical of most realisations and are not unusual cases.

Figure 5 shows in more detail the northern tangent region for the best matching realisation. The top panel shows good overall agreement in the number, distribution and sizes of spots as compared with the observations of D99 and T97. Amongst these very brightest masers, just as in the observations, there are more maser spots on the eastern side of the tangent point than the western side. This is explained by the fact that on the eastern side there is more background continuum (see Fig. 2a). Note that the middle row of Fig. 4 shows an opposite behavior on larger scales caused by the presence of the free-free absorption bicone. In a given realisation (see inset in Fig. 5) a typical spot spectrum has *FWHM* of 30 km s^{-1} and FWZI ~ 100 km s^{-1}, which is in agreement with the observations presented in D99 and T97. The brightest spot shown in Fig. 5 is caused by the partial overlap of 5 individual clouds. This spot has an LCR of ~1200 and a 1667:1665 MHz line ratio ρ = 28. Both values are consistent with the limits LCR > 500 and ρ > 20 found by D99 in their brightest spot (see Table 2).

The position-velocity diagram of the compact maser spots shown in the bottom panel of Fig. 5 shows a linear gradient of ~30±12 km s^{-1} pc^{-1} for the eastern group of spots. This is similar to the gradient of 32 km s^{-1} pc^{-1} found by D99 in their central group of maser spots (designated N2 in D99). In this model realisation no similar gradient was seen in the southern tangent region; just as is the case in the observations. This illustrates the stochastic nature of the mechanism for producing velocity gradients as described in Sect. 3.6. While our model can reproduce the overall gradient seen in the northern tangent region the dispersion we find about this gradient is significantly larger than that observed by D99. There are several possible reasons for

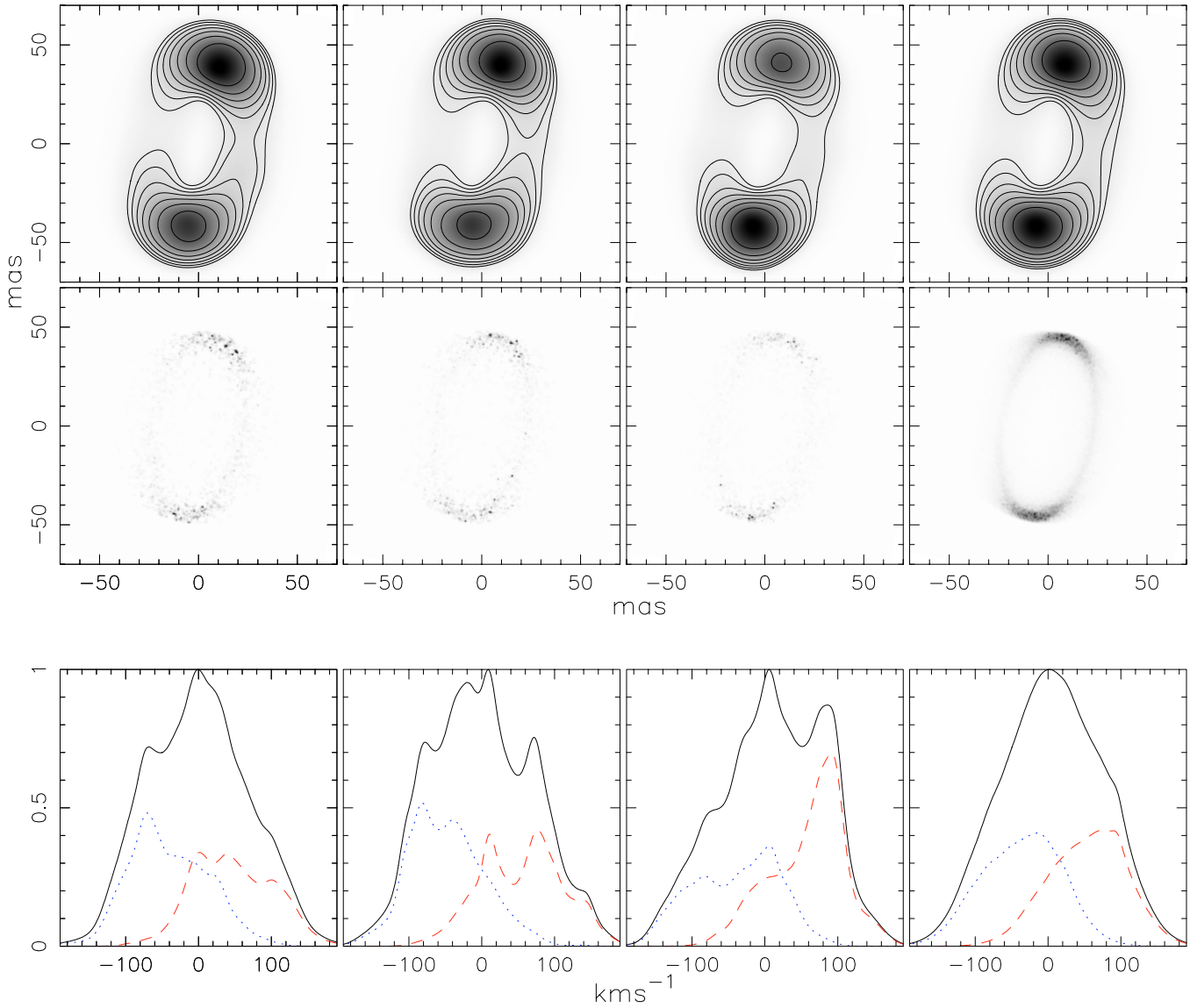

Fig. 4. The first three columns show sample realisations of the Monte-Carlo simulation. The rightmost column shows the average over 100 realisations. Intensity and flux are in arbitrary units, normalized to their peaks. Images: *top row*: greyscale and contours represent the velocity integrated OH maser emission convolved with a simulated EVN+MERLIN beam (*FWHM* $\approx$ 35 mas). Contours are logarithmically spaced from $2^{-1/2}$ to $2^{-7/2}$ of the peak. *Middle row*: Integrated emission at global VLBI resolution (*FWHM* = 0.92 mas). Spectra: the solid line is the spectrum integrated over the entire source. Dashed and dotted lines represent spectra taken at the southern and northern tangent regions respectively.

this. First it may be that better fits can be found using models with larger mean outflow velocities (i.e. larger v_z in Table 1) and smaller random components (i.e. smaller Δv and Δv_z in Table 1). Secondly the outflow velocity field we used was very crude, simply a change of sign in velocity for clouds on either side of the midplane. If clouds are instead gradually accelerated with increasing z-distance then tighter gradients might be produced. An interesting possibility is that such apparent accelerations could occur if clouds have limited lifetimes before their dissipation (see Sect. 6.1). In this case clouds emitted from the midplane with higher v_z would be observed with systematically larger z-distances. Finally our assumption of spherical clouds is unlikely to be true in reality. More systematic gradients might be produced if maser features are instead due to overlapping filaments.

5. Discussion of maser properties

5.1. High brightness temperature and maser saturation

Previous studies have argued that compact megamaser features imply saturated amplification because of the absence of detectable seed continuum and the resulting large LCRs (>500 in IIIZw35 and >800 in Arp 220; D99, L98). The high brightness temperatures of the compact spots, $T_b > 2\times10^9$ K in IIIZw35 have also been taken as evidence for saturation (D99). However, even an LCR of 800 implies maser amplification with τ of only 6.7, considerably below the typical saturation requirements of astronomical masers, $\tau \sim$12–15 (Elitzur 1992). In our model, the brightest features arise from the alignment of n = 5 maser clouds each with τ_c = 1.5 giving a total optical depth

Table 2. Observed and modeled quantities

	Observed	Model
Single dish:		
Velocity range[a] (km s^{-1})	270 ± 20	∼280
EVN+MERLIN:		
$\tau^{b}_{\rm North}$	3.85 ± 0.34	3.58
$\tau_{\rm South}$	4.30 ± 0.12	3.80
$\tau_{\rm East}$	2.66 ± 0.33	1.20
$\tau_{\rm West}$	2.26 ± 0.21	0.69
Global VLBI:		
$\tau_{\rm South}$	>6.21	7.28
FWHM of peak spot (km s^{-1})	∼30	30

[a]Velocity width of the 1667 feature at 10% of the peak flux density.
[b]The effective opacities are $\tau_{\rm North} = \ln({\rm LCR}_{\rm North})$, etc.

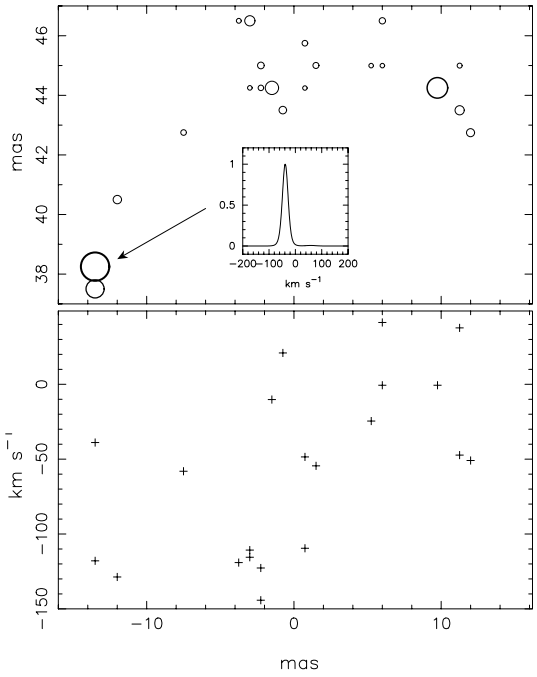

Fig. 5. *Top*: detail of the northern region of the best matching model realisation at global VLBI resolution. The diameter of the circles plotted are proportional to the maser spot velocity integrated emission. For comparison with the results of D99, only spots brighter than 5% of the peak are shown. The inset is the spectrum of the brightest feature *Bottom*: position-Velocity diagram of the brightest maser spots. The data suggests the presence of a linear gradient ∼30 ± 12 km s^{-1} pc^{-1} for spots on the eastern side of the plot.

of 7.5, well below that required for saturation. The assumption of unsaturated amplification made in the modelling is therefore self consistent even for the strongest features.

It is also important to remember that saturation depends on the angle-averaged intensity $J = I \times (\Omega/4\pi)$, so even larger brightness temperatures and LCRs are possible without saturation whenever the beaming angles Ω are small. Such small beaming angles are natural in the case of a collection of small clouds as we have in our model. If there are n spherical masers, each of optical depth $\tau_{\rm c}$ and diameter a aligned along a length L then

$$\frac{\Omega}{4\pi} = \frac{1}{16 n \tau_{\rm c}} \left(\frac{a}{L}\right)^2 . \quad (1)$$

With $a = 0.7$ pc, $\tau_{\rm c} = 1.5$ and $L \sim 13$ pc at the ring tangents, then the brightest maser spots, for which $n = 5$, have $\Omega/4\pi$ of only $\sim 2.4\times10^{-5}$. Hence maser spot brightness temperatures many orders of magnitude larger than the present limits would still be consistent with unsaturated emission. It is important to note that the tight beaming produced by lines of overlapping maser clouds is highly anisotropic. The large LCRs and brightness temperatures achieved in our model would not be observed from locations along the ring axis.

5.2. Maser line ratios

Compact masers features observed in OH megamasers display large values of $\rho = I_{1667}{:}I_{1665}$. For instance, in Arp 220, L98 find from their VLBI observations $\rho > 100$ in the brightest maser spots, in contrast with single dish spectra where ρ is only 4.2. In IIIZw35, the 1665 MHz line was detected only toward one bright feature at VLBI resolution (D99), yielding $\rho > 20$. In all other features, this maser emission is below detection.

The large observed values of ρ were a major impetus for the proposition that the compact emission is different in nature from the diffuse maser component. However, the observed difference in ρ between these two apparent phases is a natural property of clumpy unsaturated masers. If τ is the 1667 MHz optical depth of a single cloud and $R = \tau_{1667}{:}\tau_{1665}$, then n overlapping clouds will produce $\rho = \exp(n\tau \cdot [1 - 1/R])$. From an extensive compilation of OH megamaser sources, Henkel & Wilson (1990) find that $R = 1.9 \pm 0.3$ for the sample average, similar to the ratio of 1.8 if the two transitions have the same excitation temperature. For the five-cloud overlap responsible for the brightest feature in our simulation, $\rho > 20$ for $R > 1.7$, consistent with the observations. The line ratio of the velocity integrated emission from our simulated model single dish spectra is ∼4 which is comparable to the observed value from Arecibo spectra of 6.1 (Mirabel & Sanders 1987).

5.3. Broad maser lines

In order to fit the observed velocity width of the compact maser spots, our model requires clouds with an internal velocity dispersion of 20 km s^{-1}. Although fairly large, this is significantly less than if each compact maser were produced in a single unsaturated cloud, in which case line narrowing due to the high amplification would require cloud velocity widths of ∼60 km s^{-1}. In our model, line narrowing due to unsaturated maser amplification is largely canceled out by velocity broadening from combining many clouds with different velocity centres.

In bright galactic masers, the brightest spectral features are often quite narrow (<1 km s^{-1}). This might be expected from a population of individually emitting maser clouds. In that case, clouds with small velocity width would give the

strongest masers because the inverted column density is spread over a narrow velocity range so these clouds have the largest peak gains. In contrast, the linewidths of bright megamaser spots are typically several tens of km s^{-1}, and up to 150 km s^{-1} (Lonsdale 2002). Such large widths cannot arise from a population of narrow-width clouds because they would require unrealistic multi-cloud superpositions. These large widths clearly indicate spectral blending of individual clouds with internal velocity widths $\gg$1 km s^{-1}. Such blending arises naturally from cloud overlaps in a population with a distribution of internal cloud properties. Multiple cloud maser emission requires overlaps in both space and velocity, therefore narrow-velocity clouds, which rarely overlap, are selected against. The overlap of a small number of clouds with large internal velocity dispersion, and thus small peak gains, naturally leads to broad spectral lines of moderate gain.

5.4. Application of the model to other sources

Does the model proposed here apply to other sources showing both compact and diffuse maser components? The best studied OH megamaser source is Arp220, observed at global VLBI resolution (L98) and with EVN and MERLIN separately (Rovilos et al. 2003); though there is no published map using the combined data from both arrays. Arp220 shows maser emission from its West and East nuclei, with the latter showing a strong similarity to IIIZw35: bright maser emission from two well separated regions that contain about a half of the total source flux. The central velocities of the two bright regions differ by ∼100 km s^{-1}, yet their spectral ranges overlap, just as in IIIZw35. This suggests that a similar ring model might apply also to the Arp220 eastern nucleus; indeed, a rotation of the model images presented in Fig. 4 shows a striking similarity with the Arp220 maps (see Fig. 2 in L98). The northern region of the eastern nucleus contains more compact structures than the southern region, including one very bright spot. This can be readily explained in our model, which is stochastic in nature. Large velocity gradients over a short distance in the bright regions are also explained by the overlap of clouds or filaments at slightly different centre velocities. In the western nucleus of Arp 220 the difference in compactness between the northern and southern patches of emission are harder to reconcile with a rotating ring geometry, although the large LCRs (>800) and large ρ (>100) are qualitatively explained by our multiple cloud overlap model.

Another possible candidate source is Mrk273 (Klöckner et al. 2003). This source, too, shows both compact and resolved-out maser emission, and the compact emission occurs in two distinct regions with different velocity centres. The existence of these two regions can be explained by competition between the fall off of background continuum brightness as we move away from the projected ring axis versus increased path-length through the OH ring. The latter path-length increases the maser brightness almost exponentially while the continuum strength effects it only linearly.

Note that in IIIZw35, Mrk273 and Arp220 the brightest masers are not coincident with the brightest continuum, but this is not strong evidence for saturated emission as is sometimes claimed. Instead, given the exponential effect of path length on brightness in unsaturated masers it is quite feasible that the brightest emission occurs in regions where the continuum emission is very weak or presently undetectable.

6. Physical considerations

6.1. Cloud mass and confinement

Here we discuss the physical properties of our OH maser clouds. The maximum density of a OH maser emitting gas is of order $n(H_2) = 10^5$ cm^{-3}. Higher densities will thermalise the energy levels and quench the maser (Elitzur 1992). Assuming this maximum density, a OH abundance of 10^{-5} and excitation temperature 10 K, equation 9.12 in Elitzur (1992) gives a minimum cloud diameter of 0.02 pc. Assuming instead that clouds have diameters equal to the observational upper limit of 0.7 pc then the same equation gives a minimum mean hydrogen density of 3.1×10^3 cm^{-3}. This gives an upper limit for cloud mass of 24 $M_\odot$. Note however that this upper limit is critically dependant on the assumed OH abundance.

Are the OH maser clouds confined? It seems that gravitational confinement can be rejected. Given their internal velocity dispersion of 20 km s^{-1}, to be gravitationally bound the clouds would require a virial mass of $\sim 2\times10^4$ $M_\odot$. This is much larger than the upper limit estimated from OH properties. Such a cloud mass would also give a total mass in clouds of $\sim 2\times10^7$ $M_\odot$, which is larger than the dynamical mass internal to the maser ring of 7×10^6 $M_\odot$ derived from the maser kinematics (P01).

Could the clouds be pressure confined by the ionised Inter-Cloud Medium (ICM)? Using the inferred optical depth of the free-free absorbing gas and assuming it is uniformly distributed, the electron number density in the ICM is $\sim 10^3$ cm^{-3}. If the temperature of the ICM is 10^4 K, then the pressure becomes $P_{\rm ICM} \sim 10^7$ K cm^{-3}. In contrast, from the internal turbulent velocity of the clouds their inferred dynamical pressure is of order 3×10^8 K cm^{-3}, therefore they cannot be pressure confined. Finally magnetic confinement would require a magnetic field of ∼10 mG. This is feasible given the range of magnetic field strengths observed towards galactic OH masers (Reid & Moran 1981; Fiebig & Guesten 1989) if the OH masers occurred in gas of the highest possible density (i.e. near $n(H_2) = 10^5$ cm^{-3}). For comparison in IIIZw35 Zeeman splitting observations by Killeen et al. (1996) estimate an upper limit on the non-uniform magnetic field to be 5 mG, however this limit is very model dependant.

Although magnetic confinement is possible given the observational limits, it is interesting to consider models in which the clouds are freely expanding. Assuming the largest possible cloud size (0.7 pc) and dividing by the cloud internal velocity dispersion gives a characteristic cloud lifetime of $\sim 3.4 \times 10^4$ yr. Given their outflow velocity of 60 km s^{-1} in the z direction, such clouds would reach a height of ∼2.1 pc which is roughly consistent with the observed $\Delta H/2 = 3$ pc (see Table 1). An additional advantage of this model is that that the ionised free-free absorbing gas required by our model might naturally be

generated from the dissipated clouds. If the clouds have uniform density and consequently a mass of ∼24 $M_\odot$ then the total kinetic power being injected into all clouds would be about 7×10^{38} erg s^{-1} which is a very small fraction of the mechanical power available from supernova explosions (i.e. 2×10^{43} erg s^{-1}) assuming a supernova rate of 0.8 yr^{-1} (P01). Using the same cloud mass, the mass loss rate in the outflowing clouds is 0.8 $M_\odot$ yr^{-1} which is much smaller than the estimated SFR (19 $M_\odot$ yr^{-1}, see P01).

6.2. Constraints on central AGN and black hole

Our axisymmetric model (Fig. 2) suggests a central point to both the ring and the ionised outflow and it is natural to ask whether an AGN or black hole exists at this point. We should first remark that within the OH ring radius, the geometry of our model is observationally ill-defined and so the cone of free-free absorbing gas shown in Fig. 2 may not in fact extend all the way inwards to a central point. If as we argue in Sect. 6.1, the free-free absorbing gas is the remains of dissipated molecular clouds, then the free-free cone will in fact be truncated at a height comparable to the OH ring height.

Observationally there is conflicting evidence for the presence of an AGN in IIIZw35. The source lies on the well known FIR-radio correlation for starbursts (see P01) and so has no radio excess which might accompany a strong AGN. Also high resolution radio observations (see P01) do not show any compact radio features at our inferred centre. However such a radio core might be free-free absorbed at 1.6 GHz so it would be interesting to conduct higher frequency VLBI observations to check this possibility. We have not been able to find any X-ray observations which imply an AGN.

In contrast to the above C90 argued that the near-IR colours of IIIZw35 were consistent with it being a mixed starburst/AGN. Furthermore from their optical spectroscopy C90 classified IIIZw35 as a borderline LINER/Seyfert2 nucleus based on classical (semi-empirical) line ratio diagnostics. A similar analysis by Baan et al. (1998) using different optical spectroscopic observations but a similar diagnostic scheme classified IIIZw35 as a LINER. Whether galaxies classified as LINERs are primarily AGN or starburst powered is presently unclear. Using the physically based line diagnostic scheme of Kewley et al. (2001) many LINERs are reclassified as high metallicity starbursts (Corbett et al. 2003). However, taking the data for IIIZw35 from Baan et al. (1998) and applying the Kewley et al. (2001) diagnostic scheme we find that IIIZw35 still falls in the AGN region. The data is however consistent with a mixed AGN/starburst with the latter still providing most of the luminosity in the diagnostic optical lines. As noted by Corbett et al. (2003). estimating the relative bolometric AGN contribution in starbursts purely from optical emission lines is very difficult because of the large optical obscuration in these objects.

Is there any dynamical evidence for a central black hole? From the observed maser dynamics the derived enclosed mass within the OH maser ring radius of 22pc is $7{\times}10^6$ $M_\odot$. The resulting mass density of 156 $M_\odot$ pc^{-3} can easily be achieved by stars or gas within the nuclear region and so there is no necessity for a central point mass. However a moderate mass black hole is not ruled out either. The total enclosed mass in IIIZw35 could for instance be contributed equally from a black hole like the one in our galaxy (3.5×10^6 $M_\odot$, Eckart & Genzel 1997) and a distributed mass of stars. We note that even in the extreme case that such a black hole is being maximally fed, then the maximum luminosity if radiating at 10% of the Eddington limit would be 2×10^{10} $L_\odot$ which is over ten times smaller than the observed FIR luminosity. We conclude that although optical spectroscopy shows that an AGN might be present in IIIZw35 it must be energetically insignificant compared to the starburst activity.

6.3. Nature of the OH and continuum rings

We argue in the previous section that the bulk of the bolometric emission in IIIZw35 is powered by starburst activity rather than an AGN. Certainly for the radio emission its consistency with the radio-FIR correlation, its observed brightness temperature (P01) and its ring-like morphology argues for an origin in a starburst ring. Such a starburst ring can also provide the IR photons to pump OH and therefore also explain the ring morphology of the maser emission.

A remarkable property of the OH ring is its relative narrowness (see Sect. 3.3 and Table 1), which is only 12% of the radius. The fact that OH absorption is seen outside the ring and perhaps in its central hole (P01) suggests that this geometry is not defined merely by OH abundance. The most direct interpretation of the narrow maser ring is that it is defined by the range of radii over which star formation is presently occurring. Such ring can be identified as a scaled down version of the sub-kiloparsec nuclear starburst rings known to exist in many starburst galaxies (see Knapen et al. 2004, and references therein). In addition, numerical simulations of starburst-generated rings or tori have been made (Wada & Norman 2003; Wada & Tomisaka 2005) supporting the existence of circumnuclear filamentary structures. The presence of radio continuum emission at larger radii in IIIZw35 (see Fig. 1) may indicate the remnant of past star formation, in turn suggesting an inwardly propagating ring of star-formation. The fact that the OH masing clouds in the ring are not gravitationally bound to the nucleus (see Sect. 6.1) suggests that emission at any given radius must be short lived. Supernova explosions in a ring may compress dense gas on the inside of the ring causing the ring to propagate inwards.

Alternatively to the above picture, star formation in IIIZw35 may exist over a wide range of radii, rather than just in a ring, but the required conditions for population inversion might only apply over a narrow range of radii. The inversion of OH main lines is critically dependant on the local IR spectrum (Elitzur 1978; Cohen et al. 1988; Moore et al. 1988; Kegel et al. 1999), which in turn depends on the local SFR rate and Initial Mass Function.

It is interesting to compare the size and structure of our OH maser ring with other OH maser observations of circumnuclear features. In Mrk231 (Klöckner et al. 2003) an OH torus with

radius from 30 pc to 100 pc has been inferred. It follows that the inner edge of that torus is comparable in size to the ring in IIIZw35 but it extends over a larger radius and appears to be much thicker. We argue in Sect. 5.4 that the structures seen at the eastern nucleus of Arp220 (Rovilos et al. 2003) could also be explained by a thin ring with a radius of ~30 pc being very similar to IIIZw35. It appears from the observations that a wide variety of circumnulear OH maser structures can exist.

The OH torus found in Mrk 231 (Klöckner et al. 2003) has been identified with the obscuring torus required in AGN unified schemes, although the inner radii of such structures are expected to be much smaller (close to the dust sublimation radius which is sub-parsec in weak Seyferts or strong LINERS). In contrast it does not seem that the OH ring we see in IIIZw35 can directly contribute much to any such obscuration. From the direction of observation, the ring does not cover the central point where any AGN might be expected to reside. Furthermore the narrow ring covers only a small solid angle and even if it was observed edge-on, the obscuration would still be small because given the derived cloud column densities (Sect. 6.1) the expected obscuration is only $A_v \sim 1$ assuming a standard gas to dust ratio. However, it cannot be ruled out that the structure seen in OH is the outer part of a starburst supported disk which extends down to small radii where it might have a much larger geometrical and optical thickness.

7. Conclusions and future work

Observations of distinct regions of compact and apparently diffuse maser emission in OH megamasers have, in the past, been used to argue for two physical phases of OH masers (see L98, D99). In contrast, the mechanism discussed in this paper explains both types of maser structures using a single phase of low opacity clouds within a thin circumnuclear ring. The properties of the clouds are similar to those assumed in the standard model (Baan 1989) but our model explicitly considers the statistical effects of rare multi-cloud overlaps. Compared to others, our model is therefore conservative in that the physical properties of the standard model are preserved.

Despite the simplicity of our model we find that most of the observational features of IIIZw35 can be reproduced. The fact that the maser amplifying medium is composed of clouds is found essential to explain the range of maser brightness around the ring at low resolution. The same clouds also explain the bright maser spots seen only at the ring tangents in terms of multiple cloud overlaps in both space and velocity. The model is able to reproduce the LCRs in the bright spots and diffuse regions, and the large value of the 1667 MHz:1665 MHz line ratio in the compact spots. Finally it can explain the spectra of both the compact spots and the apparently diffuse areas of emission. The fact that the OH clouds are outflowing from the ring midplane explains the large velocity gradients observed amongst the compact maser spots. We find that the OH masing ring is relatively narrow in radius which could be explained either in terms of a narrow circumnuclear ring of star formation, or due to the strong sensitivity of maser pumping to physical conditions which vary gradually with radius. The ring we find is narrower but qualitatively similar to those that have been produced in numerical simulations (Wada & Norman 2002; Wada & Tomisaka 2005).

Our model can be improved in many ways. It assumes all clouds are identical, when in reality a spectrum of cloud sizes and opacities is expected. Additionally it presently assumes spherical clouds whereas computer simulations (Wada & Norman 2002) show that filamentary structures are common in starburst nuclei. These latter structures may also show outward velocity gradients due to acceleration by radiation pressure; including such filaments will give rise to higher velocity correlation between masers spots, as seen in the observations. The next step in simulations of megamaser sources might be to take the output of numerical dynamical simulations and calculate the expected OH megamaser emission.

One line of future work involves taking the estimates of cloud opacity, size, internal velocity dispersion and 1667:1665 MHz line ratio found in IIIZw35 and deriving the implications for gas physical conditions and pumping. Another important area to investigate is the general one of properties of maser emission in a cloudy medium, especially the generalisation to media with a range of cloud opacities. While much work has been put into understanding masers in simple geometries such as spheres or filaments relatively little work has been done for random media. One exception is Sobolev et al. (2003) who carried out numerical simulations of masers in continuous media with a Kolmogorov spectrum of local opacity. Multi-phase media are common in astrophysics and the case we have studied here of masers arising in discrete clouds is another limit which requires careful attention. Observationally separate regions of compact and apparently diffuse maser emission are often found in other species of galactic and circumstellar masers. Examples include galactic methanol (Minier et al. 2000) and circumstellar SiO masers (Yi et al. 2005). These core-halo structures are often interpreted in terms of single clouds which have saturated outer layers and unsaturated cores. However, such structures might also be explained by invoking the presence of a clumpy medium.

Acknowledgements. R.P. thanks the University of Kentucky for a most delightful month, which helped in bringing this paper forward to submission. J.C. gratefully acknowledges support from the Swedish science research council (VR). M.E. gratefully acknowledges the partial support of NSF. The authors acknowledge the incisive comments sent by the referee, Phil Diamond, which helped to significantly improve the manuscript.

Appendix A: Maser gain in clumpy media

Consider a population of identical unsaturated maser clouds amplifying background continuum. At a given velocity let $\bar{N}$ be the mean number of clouds which are encountered along a given LOS. If the clouds are of non-zero size and cannot interpenetrate there is also a maximum number of clouds $N_{\max}$, set by the number than can be fitted along a LOS. If the maser

optical depth of each cloud is τ_c then the mean value of the gain is

$$G_{\rm mean} = \sum_{k=0}^{N_{\rm max}} P_{\bar{N},N_{\rm max}}(k) \cdot {\rm e}^{k\tau_c}, \qquad \text{(A.1)}$$

where $P_{\bar{N},N_{\rm max}}(k)$ is the probability of having k overlaps. If the cloud volume filling factor is small such that $N_{\rm max} \gg \bar{N}$ then $P_{\bar{N},N_{\rm max}}(k)$ can be replaced by the Poisson distribution $P_{\bar{N}}(k) = \bar{N}^k {\rm e}^{-\bar{N}}/k!$ and the upper limit on the sum tends to infinity. In this case the mean of the gain is given by

$$G_{\rm mean} = \sum_{k=0}^{N_{\rm max}\to\infty} P_{\bar{N}}(k) \cdot {\rm e}^{k\tau_c} = \exp\left[\bar{N}({\rm e}^{\tau_c} - 1)\right] \qquad \text{(A.2)}$$

as found by Natta & Panagia (1984). However we find that when $\tau_c > 1$ the above expression enormously overestimates the average gains in our Monte-Carlo simulations; even for a negligible cloud filling factor. The reason is that in the above series although the Poisson probabilities $P_{\bar{N}}(k)$ decreases rapidly for $k > \bar{N}$, for $\tau_c > 1$ this decrease is more than offset by the increase of the amplification factors ${\rm e}^{k\tau_c}$. The result is that the series summation becomes dominated by very rare events with $k \gg \bar{N}$. In contrast for a typical Monte-Carlo simulation such an extreme multi-cloud overlap event is very unlikely to occur even once within any of the independent lines of sight within an interferometer beam.

An analytic expression for $G_{\rm mean}$ which is in closer agreement with our Monte-Carlo simulations can be constructed in the following way: if the interferometer beam is M times larger than a cloud area, each beam can be assumed to contain M independent lines of sight. Consequently, the series in Eq. (A.2) can be truncated at a finite $N_{\rm max}$ to exclude improbable events that are unlikely to occur even once within the beam. More accurately, $N_{\rm max}$ can be defined such that the maximum number of overlaps within a region of M lines of sight is less than $N_{\rm max}$ in 50% of realisations. This gives:

$$G_{\rm mean} \simeq \sum_{k=0}^{N_{\rm max}} P_{\bar{N}}(k) \cdot {\rm e}^{k\tau_c} \qquad N_{\rm max} = P_{\bar{N}}^{-1}\left(2^{-\frac{1}{M}}\right) \qquad \text{(A.3)}$$

where $P_{\bar{N}}^{-1}$ is the inverse Poisson cumulative distribution. Using Monte-Carlo simulations (see Fig. A.1) this equation is found to give a good approximation to the mean gain over a wide range of $\bar{N}$. Using the above definition of $N_{\rm max}$ the median value of the peak gain within a region of M independent lines of sight is given by

$$G_{\rm max} \simeq \exp(N_{\rm max} \cdot \tau_c). \qquad \text{(A.4)}$$

An important point, which is evident from Fig. A.1, is that the effective opacity $\tau_{\rm eff} = \ln(G_{\rm mean})$ shown on the scale to the right, is much larger than the mean opacity in that region $\tau_{\rm mean} = \bar{N}\tau_c$ (shown at the scale on the top). The two quantities differ because of the high k tail of the $P_{\bar{N}}$ distribution. Figure A.1 also demonstrates another remarkable property of masers in a clumpy medium, that the effective opacity $\tau_{\rm eff}$, is not linearly dependent on $\bar{N}$ but falls well below that prediction as $\bar{N}$ and $\tau_{\rm mean}$ increase. This effect arises because as $\bar{N}$ increases the variance about the mean in the number of clouds per line of sight decreases which in turn reduces the contribution from rare many-cloud overlaps. As described in Sect. 3.4 this nonlinear relationship between effective opacity and $\bar{N}$ for a clumpy media allows us to understand the otherwise puzzling variation in LCR around the maser ring.

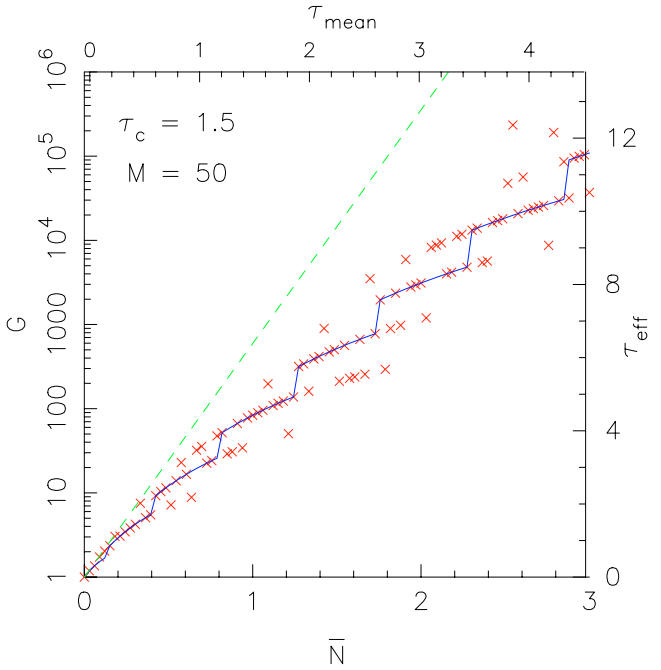

Fig. A.1. Variation of the mean gain G with the mean number $\bar{N}$ of overlapping maser clouds when the individual cloud optical depth is $\tau_c = 1.5$. The crosses show the results of a numerical Monte-Carlo calculation that averages over $M = 50$ lines of sight. The solid line is the result of analytic calculation using Eq. (A.3). The dashed line plots the result of an infinite-series summation (Eq. (A.2)). The top axis shows the distribution mean optical depth $\tau_{\rm mean} = \bar{N}\tau_c$, the right axis its effective optical depth $\tau_{\rm eff} = \ln G_{\rm mean}$.

References

Baan, W. A. 1989, ApJ, 338, 804
Baan, W. A., Salzer, J. J., & Lewinter, R. D. 1998, ApJ, 509, 633
Chapman, J. M., Staveley-Smith, L., Axon, D. J., et al. 1990, MNRAS, 244, 281
Cohen, R. J., Baart, E. E., & Jonas, J. L. 1988, MNRAS, 231, 205
Corbett, E. A., Kewley, L., Appleton, P. N., et al. 2003, ApJ, 583, 670
Diamond, P. J., Norris, R. P., Baan, W. A., & Booth, R. S. 1989, ApJ, 340, L49
Diamond, P. J., Lonsdale, C. J., Lonsdale, C. J., & Smith, H. E. 1999, ApJ, 511, 178
Eckart, A., & Genzel, R. 1997, BAAS, 29, 1366
Elitzur, M. 1978, A&A, 62, 305
Elitzur, M. 1992, Astronomical masers (Kluwer Academic Publishers), Astrophysics and Space Science Library, 170
Fiebig, D., & Guesten, R. 1989, A&A, 214, 333
Heckman, T. M. 2003, Rev. Mexi. Astron. Astrofis. Conf. Ser., 47
Henkel, C., & Wilson, T. L. 1990, A&A, 229, 431
Kegel, W. H., Hertenstein, T., & Quirrenbach, A. 1999, A&A, 351, 472

Kewley, L. J., Heisler, C. A., Dopita, M. A., & Lumsden, S. 2001, ApJS, 132, 37
Killeen, N. E. B., Staveley-Smith, L., Wilson, W. E., & Sault, R. J. 1996, MNRAS, 280, 1143
Klöckner, H., Baan, W. A., & Garrett, M. A. 2003, Nature, 421, 821
Klöckner, H.-R., & Baan, W. A. 2004, A&A, 419, 887
Knapen, J. H., Whyte, L. F., de Blok, W. J. G., & van der Hulst, J. M. 2004, A&A, 423, 481
Lonsdale, C. J. 2002, in Cosmic Masers: From Proto-Stars to Black Holes, Ed. V. Mineese and M. Reid (San Francisco, ASP), Proc. IAU Symp., 206, 413
Lonsdale, C. J., Diamond, P. J., & Smith, H. E. 1994, Nature, 370, 117
Lonsdale, C. J., Lonsdale, C. J., Diamond, P. J., & Smith, H. E. 1998, ApJ, 493, L13
Minier, V., Booth, R. S., & Conway, J. E. 2000, A&A, 362, 1093
Mirabel, I. F., & Sanders, D. B. 1987, ApJ, 322, 688
Montgomery, A. S., & Cohen, R. J. 1992, MNRAS, 254, 23
Moore, T. J. T., Mountain, C. M., Yamashita, T., & Selby, M. J. 1988, MNRAS, 234, 95
Natta, A., & Panagia, N. 1984, ApJ, 287, 228
Pihlström, Y. M., Conway, J. E., Booth, R. S., Diamond, P. J., & Polatidis, A. G. 2001, A&A, 377, 413
Reid, M. J., & Moran, J. M. 1981, ARA&A, 19, 231
Rovilos, E., Diamond, P. J., Lonsdale, C. J., Lonsdale, C. J., & Smith, H. E. 2003, MNRAS, 342, 373
Smith, H. E., Lonsdale, C. J., Lonsdale, C. J., & Diamond, P. J. 1998, ApJ, 493, L17
Sobolev, A. M., Watson, W. D., & Okorokov, V. A. 2003, ApJ, 590, 333
Staveley-Smith, L., Cohen, R. J., Chapman, J. M., Pointon, L., & Unger, S. W. 1987, MNRAS, 226, 689
Trotter, A. S., Moran, J. M., Greenhill, L. J., Zheng, X., & Gwinn, C. R. 1997, ApJ, 485, L79
Wada, K., & Norman, C. A. 2002, ApJ, 566, L21
Wada, K., & Norman, C. A. 2003, ASP Conf. Ser., 261
Wada, K., & Tomisaka, K. 2005, ApJ, 619, 93
Yi, J., Booth, R. S., Conway, J. E., & Diamond, P. J. 2005, A&A, 432, 531